Zero-gap electrolyzers accelerate reconstruction of Cu_2O-derived catalysts under CO_2 reduction

Jehad Abed[1,2†], Ivan Grigioni[2,3†], Talha Kose[4], Wajdi Alnoush[5], Sungjin Park[2], Anna Lisa Polo,[3]
Byoung-Hoon Lee[2,6], David Sinton[4], Drew Higgins[5*], and Edward H. Sargent[2*]

[1] *Department of Materials Science and Engineering, University of Toronto, 184 College Street, Toronto, Ontario M5S 3E4, Canada.*

[2] *Department of Electrical and Computer Engineering, University of Toronto, 35 St George Street, Toronto, Ontario M5S 1A4, Canada.*

[3] *Department of Chemistry, University of Milan, Via Camillo Golgi, 19, 20133 Milano MI, Italy.*

[4] *Department of Mechanical and Industrial Engineering, University of Toronto, 5 King's College Road, Toronto, ON M5S 3G8, Canada.*

[5] *Department of Chemical Engineering, McMaster University, 1280 Main Street West, Hamilton, ON L8S 4L7, Canada*

[6] *Graduate School of Converging Science and Technology, Korea University, 145, Anam-ro, Seongbuk-gu, Seoul 02481, Republic of Korea*

[†] *These authors contributed equally to this work*

* *Correspondence and requests for materials should be addressed to Edward H. Sargent (ted.sargent@utoronto.ca), and Drew Higgins (higgid2@mcmaster.ca),*

Abstract

To scale carbon dioxide reduction (CO_2R), establishing a structure-property-performance relationship of the catalyst under reaction conditions is a priority. Particularly in membrane electrode assembly (MEA) electrolyzers, knowledge about the valence state and coordination environment of the catalyst is of value, yet limited. We develop a MEA electrolyzer that utilizes X-ray absorption spectroscopy to investigate the structural evolution of Cu_2O-derived catalysts under CO_2R and compare the same catalysts in a flow cell. Additionally, we study the influence of CO reduction and incorporating Ag on the reconstruction of the catalyst. We find that the strong reduction environment in the MEA and feeding CO lead to reconstruction of Cu_2O particles, favoring higher coordination and lower oxidation states, which coincides with a shift in the reaction selectivity from C_{2+} to hydrogen. While incorporating small amounts of Ag in the catalyst restricts the reconstruction. These findings advocate for *in situ* studies in zero-gap electrolyzers.

Introduction

The design of CO_2R electrochemical cells has been refined to enhance energy efficiency and product selectivity. Initially, aqueous electrolyte cells with dissolved CO_2 were used [1–3], however, the limited solubility of CO_2 in aqueous electrolytes (*ca.* 33 mM at standard condition) restricts CO_2 availability at the electrode and limits the current density to *ca.* <20 mA cm^{-2} [4,5]. Moreover, aqueous electrolytes provide an abundant source of protons, which can lead to the undesired hydrogen evolution reaction (HER) [6].

CO_2 flow electrolyzers, where separate streams of electrolyte flow past the cathode (catholyte) and anode (anolyte), offer improved mass transport of reactants to and products away from the electrode surfaces, thereby improving the reaction rate [7,8]. This makes them candidates for industrial scale applications of CO_2 electrolysis[7,8] In particular, zero-gap MEA electrolyzers feature a thin ion exchange membrane separating the cathode and anode, reducing ohmic losses and the full-cell voltage required to drive the electrochemical reaction compared to flow cells, which can experience larger ohmic losses due to electrolyte resistance within the larger fluid channels. However, electrolyzers, including MEA, alter the local reaction environment within the catalyst layer and by extension, the properties of the catalyst, which significantly affect catalytic behavior [9–12]. Generally, the active state of the catalyst in electrocatalytic cells, specially MEA, during CO_2R remains to be fully investigated and continues to be a subject of debate. [13–17].

X-ray absorption spectroscopy (XAS) provides an opportunity to probe the local chemistry of catalysts *in situ* during the reaction, specially in aqueous flow electrolyzers [4]. However, deploying *in situ* XAS to study the catalyst in a MEA electrolyzer presents additional challenges[18]. In particular, the zero-gap configuration of the MEA electrolyzer requires that the cathode/membrane/anode stack is compressed between two bipolar plates to reduce interfacial contact resistance and prevent electrolyte and gas leakages, which is not required in conventional aqueous flow cells. The bipolar plates must also contain flow fields to transport reactants (e.g., CO_2, water) to the catalyst layer. These additional features of the MEA pose challenges for *in situ* XAS because the compressed stack and bipolar plates can attenuate the X-ray beam, making it difficult to obtain clean and accurate measurements.

In this study, we devised a MEA electrolyzer that allows XAS probing of the catalyst without considerable attenuation in signal. Using the designed cell, we investigated the structural stability of Cu_2O-derived catalyst *in situ* during CO_2R at 200 mA cm^{-2}. We found that the cell architecture (MEA vs flow cell) strongly affected the structure and performance of the catalysts. Additionally, we studied the effect of reactant type (CO_2 vs CO) and the incorporation of Ag on the reconstruction behavior of the catalyst.

We designed our *in situ* XAS cell (**Figure 1**) leveraging knowledge from previous advances in the fuel cell community[19–23]. A corrosion-resistant stainless steel front plate and a Ti back plate ,electrochemically stable under harsh anodic oxidative condition, form the conductive body of the cell and sandwich the MEA. The stainless steel front plate features a stepped edge X-ray window-frame that allows a wide range of incident photon angles and reduces escape-cone losses of fluorescence X-rays (**Figure 1a**). The stainless steel plate supports a specially machined, conductive graphite plate, which is step engraved and milled as thin as 300 µm to enable X-ray penetration with a low mass attenuation coefficient (μ/ρ) at the K-edge energy of Cu and Ag. Additional details regarding the experimental setup of the cell and the preparation of the catalysts can be found in the supplementary information (**Figures S1 and S2**).

We synthesized Cu_2O via wet chemistry and Cu_2O-Ag via galvanic exchange, as detailed in the Supporting Information and in our previous work[24]. During the synthesis of the Cu_2O-Ag sample, Ag^{1+} from the reaction solution displaces Cu^{1+}, leading to surface Ag^0 (**Figure S3**) and Cu^{2+} in solution. The two nano-powders consist of porous, spherical 300 nm aggregates comprising smaller cuprite crystallites (**Figures S4 and S5**). The powders are mixed with Nafion in methanol and subsequently sprayed onto a gas diffusion electrode (GDE), as outlined in the Supplementary Information. During sample preparation, the powder aggregates break apart, forming a continuous, porous network of 70-100 nm fragments (**Figure S5**).

We then tested Cu_2O and Cu_2O-Ag GDEs in three different reaction configurations (**Figure 2a**): CO_2R in a flow cell, CO_2R in a MEA, and COR in a flow cell. In a CO_2R flow cell configuration, both Cu_2O-Ag and Cu_2O derived-catalysts produced significant amounts of C_{2+} products from CO_2R at 200 mA cm^{-2}. Galvanic replacement with Ag increased the Faradaic Efficiency (FE) towards C_{2+} by 14% (**Figure 2b** and **Tables S1-2**) and decreased FE towards CO by 13%. This is likely due to the role of Ag increasing the local concentration of adsorbed intermediate CO species (*CO) on the catalyst surface[25] and promoting *CO coupling favouring C_{2+} products [26]. However, when the catalysts were tested in the MEA electrolyzer, the selectivity for CO_2R products was substantially reduced compared to the flow cell configuration. The FE for H_2 increased from 21 to 83% for Cu_2O and from 13 to 67% for Cu_2O-Ag [27].

Next, we probed the catalysts using *in situ* XAS to determine changes to the oxidation state and coordination environment of the catalysts under CO_2R (**Figure 3**). We used commercial Cu foil, CuO and Cu_2O as reference materials for the calibration of the K-edge adsorption energies of Cu^0, Cu^{1+}, and Cu^{2+} as shown by the X-ray absorption near edge structure (XANES) analysis in **Figure 3a**. The Cu K-edge XANES spectrum showed a 0.58 eV shift toward lower energies for the Cu_2O-Ag compared to the Cu_2O (**Figure 3c**) suggesting that the overall oxidation state of Cu is slightly reduced upon Ag doping. To examine this closer, we used Fourier transform to generate a radial distribution function (RDF) from extended X-ray absorption fine structure (EXAFS) spectra (**Figure 3, right panel)**. Both Cu_2O and Cu_2O-Ag (**Figure 3d**) showed a peak for Cu-O at approximately 1.5 Å, consistent with a 1+ oxidation state, similar to the Cu_2O standard (**Figure 3b**). However, the Cu-O bond length in Cu_2O-Ag was stretched by 0.18 Å, further indicating that Cu sites experienced reduction. This was also accompanied by a drop in the coordination number (CN) of Cu-O from 2.04 in Cu_2O to 1.88 in Cu_2O-Ag, which could be a result of single-atom displacement of Cu with Ag (**Table 1 and Table 2**).

To quantify the oxidation state distribution in the as-prepared catalysts, we performed linear combination fitting (LCF) on the XANES spectra (**Figure 4**). LCA fitting showed that the samples consisted primarily of more than 65 wt.% Cu^{1+} while the rest was Cu^{2+}. The presence of Cu^{2+} is attributed to oxidation during sample preparation and storage in air.

Next, we incorporated the catalyst into a flow cell to study changes in the oxidation state and coordination environment during CO_2R. It is crucial to highlight that the pumping of the catholyte over the catalyst in flow cells can cause mechanical vibrations and minor sample movements leading to X-ray absorption perturbations, potentially diminishing the quality of EXAFS measurements. This may result in errors in the EXAFS fit with broader peaks potentially arising from measurement noise. To mitigate this, we collected and averaged additional spectra for the flow cell configurations to reduce noise compared to the MEA experiments. We have now clarified this in the manuscript to address your point. When we ran the reaction at 200 mA cm^{-2} (at -1.9 V *vs*. the reversible hydrogen electrode, not iR corrected), we found that the pre-edge XANES intensity for both Cu_2O and Cu_2O-Ag was significantly increased and the white line (peak centered at 8995 eV) was decreased, indicating the reduction of Cu. The LCF analysis showed that >92 wt.% of the Cu species were reduced to Cu^0 for Cu_2O, and <60 wt.% were reduced in Cu_2O-Ag. By examining EXAFS (**Figure 3f**), we noticed that the Cu-O peak at 1.5 Å in Cu_2O disappeared while a new peak at 2.2 Å emerged, implying that Cu_2O was reduced to metallic Cu that is undercoordinated with CN=6.03.

Despite the harsh reduction potential applied on the samples, Cu-O sites in Cu_2O-Ag experienced little reconstruction (the coordination number remained close to 2 before and during reaction) and preserved a more significant portion of their initial oxidation state compared to Cu_2O (see **Table 1 and Table 2**). To examine this closer, we used time resolved XANES to track the evolution of the oxidation state for Cu (**Figure 5**). We found that for the Cu_2O-Ag sample, Cu remained partially oxidized for at least 40 minutes, while the white oxide peak for Cu_2O faded within 2-4 minutes reducing to metallic Cu as evident by the shift of the Cu K-edge toward 8979 eV. Conducting similar time-resolved experiments with the MEA setup was challenging due to greater signal attenuation, hindering XAS data collection. Modifying the graphite plate is needed, highlighting a direction for future research.

The porous structure of both Cu_2O and Cu_2O-Ag GDEs was still preserved after the reaction in the flow cell as shown by SEM images in **Figures S5, S6a, and S6d**. SAED analysis revealed that Cu_2O experienced a more pronounced reduction than Cu_2O-Ag, as indicated by the brighter metallic copper diffraction spots and the diminished diffraction ring signal for cuprite (**Figures S6c and S6f**) which agrees with the XAS analysis.

We then used the in situ MEA electrolyzer to observe the behavior of the catalysts in the MEA configuration (**Figure 3g-h**). The absence of the catholyte in this configuration minimizes the noise observed in the flow cell. The enhanced signal-to-noise ratio in MEA cells is a desirable feature as it enables the acquisition of high-quality XAS data *in situ* for electrochemical reactions.

The XANES profiles for Cu_2O and Cu_2O-Ag in the flow and MEA electrolyzers looked similar at 200 mA cm^{-2} (**Figure 3g**). However, EXAFS analysis (**Figure 3h**) revealed that both catalysts were reduced as evident by the emergence of a metallic Cu-Cu peak at 2.2 Å and the extended structures after 4.5 Å, which could also be seen in the reference Cu foil (**Figures 3b**).

This was also confirmed by the LCF analysis (**Figure 4**), where > 90 wt.% of Cu^{1+} was reduced to Cu^0 for both Cu_2O-Ag and Cu_2O. The increase in peak intensity for the Cu-Cu bond at 2.2 Å indicates a change to the coordination environment due to substantial catalyst reconstruction in the MEA cell (**Table 1 and Table 2**). The coordination number of Cu-Cu in the Cu_2O sample was 11 during CO_2R, which is close to the value of reference metallic Cu foil (CN = 12). SEM images show that running Cu_2O-Ag GDE in MEA electrolyzer created large Cu fragments (**Figures S6g** and **S6h)**. These findings further corroborate that the catalysts undergo significant structural transformations during CO_2R in the MEA.

We switched the gas feed in a flow cell from CO_2 to CO to study the impact of CO on catalyst reconstruction (**Figure 2b**). This increased the FE to more than 90% for C_{2+} products (*ca.* 40% increase compared to CO_2R) for both Cu_2O and Cu_2O-Ag, due to the CO-rich reaction environment [28,29]. The two catalysts displayed high specific selectivity toward acetate (23% FE for Cu_2O and 37% FE for Cu_2O-Ag) implying significant changes to the reaction pathway when using CO as a reactant instead of CO_2. We found, in our previous works, that this is ascribed to larger *CO and carboxylate ($*COO^-$) intermediates adsorption favoring the acetate reaction pathway and catholyte alkalinity which provides improved energetics for C_{2+} formation [24,30].

In situ XAS under COR showed that both catalysts Cu_2O and Cu_2O-Ag were largely reduced as indicated by the well-defined pre-edge peak and the rise of an intense Cu-Cu peak at 2.2 Å (**Figures 3i and 3j**). Moreover, the coordination numbers for Cu_2O (CN=9.82) and Cu_2O-Ag (CN=10.14) during COR were much higher than CO_2R in flow cell under similar reaction conditions (**Table 1**) suggesting that the catalysts had undergone stronger reduction in COR than CO_2R. This could be ascribed to the high local concentration of CO on the catalyst surface in COR, which can adversely affect the structural stability of Cu. We also propose that any Cu-O sites that were electronically isolated within the Cu_2O-Ag electrode could have been reduced due to the inherent reducing capabilities of CO [15].

Our observations from the XAS studies shed light on the behavior of Cu_2O-derived catalysts during CO_2R and COR. It revealed that the choice of cell configuration (aqueous flow electrolyte vs. solid polymer membrane cells) and reactant type (CO_2 vs CO) significantly influenced the stability of Cu^{1+} species during the reaction.

We attribute the observed differences in the oxidation state of Cu between the different reactor configurations to the distinct reaction environments in the MEA electrolyzer and flow cells. The serpentine flow field design of the MEA electrolyzer helps facilitate a uniform interaction between reactants and the electrode. This promotes an evenly distributed current density across the catalyst, reducing more Cu^{1+} sites to Cu^0. Conversely, catalysts in flow cells can exhibit non-uniform current distributions due to variations in reactant concentration or poor electronic conductivity across the catalyst layer. This results in inconsistent reconstruction behavior of Cu at different catalyst locations. Iglesias *et al.* employed IR thermography to investigate the electrocatalytic activity of GDE in flow cell electrolyzers, noting significant temperature variations across the catalyst during CO_2R [31]. These variations, stemming from spatial differences in localized current density, can lead to uneven catalyst reconstruction.

During the CO_2R reaction in a flow cell, we noted that Cu did not fully reduce but remained partially oxidized for both Cu_2O and Cu_2O-Ag. Interestingly, incorporating small amounts of Ag in Cu_2O, had restricted the reconstruction of the catalyst during the reaction. Spatial confinement of reaction intermediates on the catalyst's surface,[32] and the presence of dispersed Ag atoms in the Cu_2O-Ag surface could have prevented the further reduction of Cu^{1+} species and the reconstruction of the surface, trapping metastable Cu-O-Ag sites [33,34]. Additionally, we conjecture that CO_2R predominantly took place at metallic (reduced) Cu atoms adjacent to Ag atoms (Cu-Ag) on the surface. Meanwhile, a portion of Cu-based atoms (or particles) stayed oxidized and electronically isolated, rendering them electro-catalytically inactive [35].

Moreover, we found that Cu_2O in both the MEA electrolyzer during CO_2R and the flow cell during COR was reduced to metallic Cu, which significantly increased the coordination number. Although Cu in both scenarios had a similar valence state and coordination number, the selectivity of these two reactions was significantly different. COR predominantly produced C2+ products with high FE, whereas CO_2R in the MEA primarily led to HER. The notable shift in FE indicates a substantial change in the accessibility of reactants to the active sites (mass transport) in the MEA configuration compared to the flow cell, contributing to the pronounced differences in HER selectivity. However, factors such as increased ionic conductivity in the MEA can lead to a higher salt concentration near the catalyst surface, affecting the reaction microenvironment. This, in turn, can cause local pH variations, which significantly influence the selectivity of the reaction [36–39]. There is also the possibility that CO_2R and COR had occurred at different active sites along the catalytic pathway to the products. This has been experimentally confirmed by Gao *et al.* using labeling experiments with mixed CO_2/CO gas feeds and *operando* Raman spectroscopy [40]. They showed that CO adsorbed on defective Cu sites is at least six times more active towards C2+ than CO_2 on Cu sites. Nonetheless, a detailed investigation of these additional factors extends beyond the scope of this current study and has been addressed in other research works [36–40].

These findings highlight the importance of utilizing *in situ* zero-gap electrolyzers to gain insights into the reconstruction mechanisms of catalysts under industrial operating conditions.

Notes

The authors declare no competing financial interests.

Acknowledgment

We acknowledge the European Synchrotron Radiation Facility (ESRF) for provision of synchrotron radiation facilities and we would like to thank Dr. Viktoriia Saveleva and Dr. Pieter Glatzel for assistance and support in using beamline ID26 during the experimental session MA5352 (https://doi.org/10.15151/ESRF-ES-744180074). J. A. acknowledges the Natural Sciences and Engineering Research Council (NSERC) of Canada under a Vanier Canada Graduate Scholarship (grant no. 705992). I.G. acknowledges the European Union’s Horizon 2020 research and innovation programme under a Marie Sklodowska-Curie grant (agreement no. 846107) and the Università degli Studi di Milano for grant CLHC

(PSR_Linea4). The authors also acknowledge support from the Alliance for AI-Accelerated Materials discovery (A3MD), which includes funding from Total Energies SE., Microsoft, and LG AI Research.

Supporting Information

Materials, Catalysts synthesis, Gas diffusion electrode (GDE) preparation, Flow cell setup for electrocatalytic measurements and XAS experiments, MEA setup, MEA electrocatalytic measurements, Anode flow field and anode catalyst for the *in situ* MEA electrolyzer, Graphite plate for the *in situ* MEA electrolyzer, Installation and experimental configuration of the MEA electrolyzer and flow cell for in situ XAS, Gas and liquid products analysis, Electron microscopy.

References

(1) Murata, A.; Hori, Y. Product Selectivity Affected by Cationic Species in Electrochemical Reduction of CO2 and CO at a Cu Electrode. *Bull Chem Soc Jpn* **1991**, *64* (1), 123–127. https://doi.org/10.1246/BCSJ.64.123.

(2) Kuhl, K. P.; Cave, E. R.; Abram, D. N.; Jaramillo, T. F. New Insights into the Electrochemical Reduction of Carbon Dioxide on Metallic Copper Surfaces. *Energy Environ Sci* **2012**, *5* (5), 7050–7059. https://doi.org/10.1039/C2EE21234J.

(3) Whipple, D. T.; Kenis, P. J. A. Prospects of CO2 Utilization via Direct Heterogeneous Electrochemical Reduction. *Journal of Physical Chemistry Letters* **2010**, *1* (24), 3451–3458. https://doi.org/10.1021/JZ1012627/ASSET/IMAGES/MEDIUM/JZ-2010-012627_0004.GIF.

(4) Clark, E. L.; Resasco, J.; Landers, A.; Lin, J.; Chung, L. T.; Walton, A.; Hahn, C.; Jaramillo, T. F.; Bell, A. T. Standards and Protocols for Data Acquisition and Reporting for Studies of the Electrochemical Reduction of Carbon Dioxide. *ACS Catal* **2018**, *8* (7), 6560–6570. https://doi.org/10.1021/ACSCATAL.8B01340/ASSET/IMAGES/LARGE/CS-2018-01340U_0008.JPEG.

(5) Higgins, D.; Hahn, C.; Xiang, C.; Jaramillo, T. F.; Weber, A. Z. Gas-Diffusion Electrodes for Carbon Dioxide Reduction: A New Paradigm. *ACS Energy Lett* **2019**, *4* (1), 317–324. https://doi.org/10.1021/ACSENERGYLETT.8B02035/ASSET/IMAGES/LARGE/NZ-2018-02035T_0001.JPEG.

(6) Higgins, D.; Hahn, C.; Xiang, C.; Jaramillo, T. F.; Weber, A. Z. Gas-Diffusion Electrodes for Carbon Dioxide Reduction: A New Paradigm. *ACS Energy Lett* **2019**, *4* (1), 317–324. https://doi.org/10.1021/ACSENERGYLETT.8B02035/ASSET/IMAGES/MEDIUM/NZ-2018-02035T_0004.GIF.

(7) Gabardo, C. M.; O'Brien, C. P.; Edwards, J. P.; McCallum, C.; Xu, Y.; Dinh, C. T.; Li, J.; Sargent, E. H.; Sinton, D. Continuous Carbon Dioxide Electroreduction to Concentrated Multi-Carbon Products Using a Membrane Electrode Assembly. *Joule* **2019**, *3* (11), 2777–2791. https://doi.org/10.1016/J.JOULE.2019.07.021.

(8) Dinh, C. T.; Burdyny, T.; Kibria, G.; Seifitokaldani, A.; Gabardo, C. M.; Pelayo García De Arquer, F.; Kiani, A.; Edwards, J. P.; De Luna, P.; Bushuyev, O. S.; Zou, C.; Quintero-Bermudez, R.; Pang, Y.; Sinton, D.; Sargent, E. H. CO2 Electroreduction to Ethylene via Hydroxide-Mediated Copper Catalysis at an Abrupt Interface. *Science (1979)* **2018**, *360* (6390), 783–787. https://doi.org/10.1126/SCIENCE.AAS9100/SUPPL_FILE/AAS9100-DINH-SM.PDF.

(9) Xu, Q.; Garg, S.; Moss, A. B.; Mirolo, M.; Chorkendorff, I.; Drnec, J.; Seger, B. Identifying and Alleviating the Durability Challenges in Membrane-Electrode-Assembly Devices for High-Rate CO Electrolysis. *Nat Catal* **2023**. https://doi.org/10.21203/RS.3.RS-2491212/V1.

(10) Vennekoetter, J. B.; Sengpiel, R.; Wessling, M. Beyond the Catalyst: How Electrode and Reactor Design Determine the Product Spectrum during Electrochemical CO2 Reduction. *Chemical Engineering Journal* **2019**, *364*, 89–101. https://doi.org/10.1016/j.cej.2019.01.045.

(11) Kim, J. Y. 'Timothy'; Sellers, C.; Hao, S.; Senftle, T. P.; Wang, H. Different Distributions of Multi-Carbon Products in CO2 and CO Electroreduction under Practical Reaction Conditions. *Nature Catalysis 2023 6:12* **2023**, *6* (12), 1115–1124. https://doi.org/10.1038/s41929-023-01082-4.

(12) Choi, W.; Chae, Y.; Liu, E.; Kim, D.; Drisdell, W. S.; Oh, H. S.; Koh, J. H.; Lee, D. K.; Lee, U.; Won, D. H. Exploring the Influence of Cell Configurations on Cu Catalyst Reconstruction during CO2 Electroreduction. *Nature Communications 2024 15:1* **2024**, *15* (1), 1–11. https://doi.org/10.1038/s41467-024-52692-w.

(13) Wang, X.; Klingan, K.; Klingenhof, M.; Möller, T.; Ferreira de Araújo, J.; Martens, I.; Bagger, A.; Jiang, S.; Rossmeisl, J.; Dau, H.; Strasser, P. Morphology and Mechanism of Highly Selective Cu(II) Oxide Nanosheet Catalysts for Carbon Dioxide Electroreduction. *Nature Communications 2021 12:1* **2021**, *12* (1), 1–12. https://doi.org/10.1038/s41467-021-20961-7.

(14) Vavra, J.; Shen, T. H.; Stoian, D.; Tileli, V.; Buonsanti, R. Real-Time Monitoring Reveals Dissolution/Redeposition Mechanism in Copper Nanocatalysts during the Initial Stages of the CO2 Reduction Reaction. *Angewandte Chemie International Edition* **2021**, *60* (3), 1347–1354. https://doi.org/10.1002/ANIE.202011137.

(15) Wilde, P.; O'Mara, P. B.; Junqueira, J. R. C.; Tarnev, T.; Benedetti, T. M.; Andronescu, C.; Chen, Y. T.; Tilley, R. D.; Schuhmann, W.; Gooding, J. J. Is Cu Instability during the CO2 Reduction Reaction Governed by the Applied Potential or the Local CO Concentration? *Chem Sci* **2021**, *12* (11), 4028–4033. https://doi.org/10.1039/D0SC05990K.

(16) Hung, S. F.; Wu, F. Y.; Lu, Y. H.; Lee, T. J.; Tsai, H. J.; Chen, P. H.; Lin, Z. Y.; Chen, G. L.; Huang, W. Y.; Zeng, W. J. Operando X-Ray Absorption Spectroscopic Studies of the Carbon Dioxide Reduction Reaction in a Modified Flow Cell. *Catal Sci Technol* **2022**, *12* (9), 2739–2743. https://doi.org/10.1039/D2CY00220E.

(17) Yang, Y.; Louisia, S.; Yu, S.; Jin, J.; Roh, I.; Chen, C.; Fonseca Guzman, M. V.; Feijóo, J.; Chen, P. C.; Wang, H.; Pollock, C. J.; Huang, X.; Shao, Y. T.; Wang, C.; Muller, D. A.; Abruña, H. D.; Yang, P. Operando Studies Reveal Active Cu Nanograins for CO2 Electroreduction. *Nature 2023 614:7947* **2023**, *614* (7947), 262–269. https://doi.org/10.1038/s41586-022-05540-0.

(18) Moss, A. B.; Hätinen, J.; Kúš, P.; Garg, S.; Mirolo, M.; Chorkendorff, I.; Seger, B.; Drnec, J. Versatile High Energy X-Ray Transparent Electrolysis Cell for Operando Measurements. *J Power Sources* **2023**, *562*. https://doi.org/10.1016/j.jpowsour.2023.232754.

(19) Segre, C.; Smotkin, E. Operando X-Ray Absorption and Infrared Fuel Cell Spectroscopy. *Electrochim Acta* **2011**, 8827–8832.

(20) Gilbert, J. A.; Kariuki, N. N.; Wang, X.; Kropf, A. J.; Yu, K.; Groom, D. J.; Ferreira, P. J.; Morgan, D.; Myers, D. J. Pt Catalyst Degradation in Aqueous and Fuel Cell Environments Studied via In-Operando Anomalous Small-Angle X-Ray Scattering. *Electrochim Acta* **2015**, *173*, 223–234. https://doi.org/10.1016/J.ELECTACTA.2015.05.032.

(21) Leach, A. S.; Hack, J.; Amboage, M.; Diaz-Moreno, S.; Huang, H.; Cullen, P. L.; Wilding, M.; Magliocca, E.; Miller, T. S.; Howard, C. A.; Brett, D. J. L.; Shearing, P. R.; McMillan, P. F.; Russell, A. E.; Jervis, R. A Novel Fuel Cell Design for Operando Energy-Dispersive x-Ray Absorption Measurements. *Journal of Physics: Condensed Matter* **2021**, *33* (31), 314002. https://doi.org/10.1088/1361-648X/AC0476.

(22) Viswanathan, R.; Liu, R.; Smotkin, E. S. In Situ X-Ray Absorption Fuel Cell. *Review of Scientific Instruments* **2002**, *73* (5), 2124–2127. https://doi.org/10.1063/1.1472469.

(23) Nakanishi, K.; Kato, D.; Arai, H.; Tanida, H.; Mori, T.; Orikasa, Y.; Uchimoto, Y.; Ohta, T.; Ogumi, Z. Novel Spectro-Electrochemical Cell for in Situ / Operando Observation of Common

Composite Electrode with Liquid Electrolyte by X-Ray Absorption Spectroscopy in the Tender X-Ray Region. *Review of Scientific Instruments* **2014**, *85* (8). https://doi.org/10.1063/1.4891036/596034.

(24) Dorakhan, R.; Grigioni, I.; Lee, B.-H.; Ou, P.; Abed, J.; O'Brien, C.; Sedighian Rasouli, A.; Plodinec, M.; Miao, R. K.; Shirzadi, E.; Wicks, J.; Park, S.; Lee, G.; Zhang, J.; Sinton, D.; Sargent, E. H. A Silver–Copper Oxide Catalyst for Acetate Electrosynthesis from Carbon Monoxide. *Nature Synthesis 2023 2:5* **2023**, *2* (5), 448–457. https://doi.org/10.1038/s44160-023-00259-w.

(25) Higgins, D.; Landers, A. T.; Ji, Y.; Nitopi, S.; Morales-Guio, C. G.; Wang, L.; Chan, K.; Hahn, C.; Jaramillo, T. F. Guiding Electrochemical Carbon Dioxide Reduction toward Carbonyls Using Copper Silver Thin Films with Interphase Miscibility. *ACS Energy Lett* **2018**, *3* (12), 2947–2955. https://doi.org/10.1021/ACSENERGYLETT.8B01736/SUPPL_FILE/NZ8B01736_SI_001.PDF.

(26) Li, Y. C.; Wang, Z.; Yuan, T.; Nam, D. H.; Luo, M.; Wicks, J.; Chen, B.; Li, J.; Li, F.; De Arquer, F. P. G.; Wang, Y.; Dinh, C. T.; Voznyy, O.; Sinton, D.; Sargent, E. H. Binding Site Diversity Promotes CO2 Electroreduction to Ethanol. *J Am Chem Soc* **2019**, *141* (21), 8584–8591. https://doi.org/10.1021/JACS.9B02945/SUPPL_FILE/JA9B02945_SI_002.PDF.

(27) Hoang, T. T. H.; Verma, S.; Ma, S.; Fister, T. T.; Timoshenko, J.; Frenkel, A. I.; Kenis, P. J. A.; Gewirth, A. A. Nanoporous Copper-Silver Alloys by Additive-Controlled Electrodeposition for the Selective Electroreduction of CO2 to Ethylene and Ethanol. *J Am Chem Soc* **2018**, *140* (17), 5791–5797. https://doi.org/10.1021/JACS.8B01868/SUPPL_FILE/JA8B01868_SI_001.PDF.

(28) Verdaguer-Casadevall, A.; Li, C. W.; Johansson, T. P.; Scott, S. B.; McKeown, J. T.; Kumar, M.; Stephens, I. E. L.; Kanan, M. W.; Chorkendorff, I. Probing the Active Surface Sites for CO Reduction on Oxide-Derived Copper Electrocatalysts. *J Am Chem Soc* **2015**, *137* (31), 9808–9811. https://doi.org/10.1021/JACS.5B06227/SUPPL_FILE/JA5B06227_SI_001.PDF.

(29) Li, C. W.; Ciston, J.; Kanan, M. W. Electroreduction of Carbon Monoxide to Liquid Fuel on Oxide-Derived Nanocrystalline Copper. *Nature* **2014**, *508* (7497), 504–507. https://doi.org/10.1038/nature13249.

(30) Wang, L.; Nitopi, S. A.; Bertheussen, E.; Orazov, M.; Morales-Guio, C. G.; Liu, X.; Higgins, D. C.; Chan, K.; Nørskov, J. K.; Hahn, C.; Jaramillo, T. F. Electrochemical Carbon Monoxide Reduction on Polycrystalline Copper: Effects of Potential, Pressure, and PH on Selectivity toward Multicarbon and Oxygenated Products. *ACS Catal* **2018**, *8* (8), 7445–7454. https://doi.org/10.1021/ACSCATAL.8B01200/SUPPL_FILE/CS8B01200_SI_001.PDF.

(31) Iglesias Van Montfort, H. P.; Burdyny, T. Mapping Spatial and Temporal Electrochemical Activity of Water and CO2Electrolysis on Gas-Diffusion Electrodes Using Infrared Thermography. *ACS Energy Lett* **2022**, *7* (8), 2410–2419. https://doi.org/10.1021/ACSENERGYLETT.2C00984/ASSET/IMAGES/LARGE/NZ2C00984_0005.JPEG.

(32) Yang, P. P.; Zhang, X. L.; Gao, F. Y.; Zheng, Y. R.; Niu, Z. Z.; Yu, X.; Liu, R.; Wu, Z. Z.; Qin, S.; Chi, L. P.; Duan, Y.; Ma, T.; Zheng, X. S.; Zhu, J. F.; Wang, H. J.; Gao, M. R.; Yu, S. H. Protecting Copper Oxidation State via Intermediate Confinement for Selective CO2 Electroreduction to C2+ Fuels. *J Am Chem Soc* **2020**, *142* (13), 6400–6408. https://doi.org/10.1021/JACS.0C01699/ASSET/IMAGES/MEDIUM/JA0C01699_M003.GIF.

(33) Tan, X.; Sun, K.; Zhuang, Z.; Hu, B.; Zhang, Y.; Liu, Q.; He, C.; Xu, Z.; Chen, C.; Xiao, H.; Chen, C. Stabilizing Copper by a Reconstruction-Resistant Atomic Cu-O-Si Interface for Electrochemical CO2 Reduction. *J Am Chem Soc* **2023**, *145*, 8664. https://doi.org/10.1021/JACS.3C01638/ASSET/IMAGES/LARGE/JA3C01638_0005.JPEG.

(34) Jeong, H.; Shin, D.; Kim, B. S.; Bae, J.; Shin, S.; Choe, C.; Han, J. W.; Lee, H. Controlling the Oxidation State of Pt Single Atoms for Maximizing Catalytic Activity. *Angewandte Chemie - International Edition* **2020**, *59* (46), 20691–20696. https://doi.org/10.1002/ANIE.202009776.

(35) Zhang, C.; Eraky, H.; Tan, S.; Hitchcock, A.; Higgins, D. In Situ Studies of Copper-Based CO2 Reduction Electrocatalysts by Scanning Transmission Soft X-Ray Microscopy. *ACS Nano* **2023**, *17* (21), 21337–21348. https://doi.org/10.1021/ACSNANO.3C05964/SUPPL_FILE/NN3C05964_SI_001.PDF.

(36) Pan, B.; Wang, Y.; Li, Y. Understanding and Leveraging the Effect of Cations in the Electrical Double Layer for Electrochemical CO2 Reduction. *Chem Catalysis* **2022**, *2* (6), 1267–1276. https://doi.org/10.1016/J.CHECAT.2022.03.012.

(37) Marcandalli, G.; Monteiro, M. C. O.; Goyal, A.; Koper, M. T. M. Electrolyte Effects on CO2Electrochemical Reduction to CO. *Acc Chem Res* **2022**, *55* (14), 1900–1911. https://doi.org/10.1021/ACS.ACCOUNTS.2C00080/ASSET/IMAGES/LARGE/AR2C00080_0005.JPEG.

(38) Disch, J.; Bohn, L.; Metzler, L.; Vierrath, S. Highlighting a Review on Strategies for the Mitigation of Salt Precipitation in Alkaline Zero-Gap CO2 Electrolyzers, Presented by the Strategies for the Mitigation of Salt Precipitation in Zero-Gap CO 2 Electrolyzers Producing CO. *J. Mater. Chem. A* **2023**, *11*, 207890. https://doi.org/10.1039/d2ta09966g.

(39) Sassenburg, M.; Kelly, M.; Subramanian, S.; Smith, W. A.; Burdyny, T. Zero-Gap Electrochemical CO 2 Reduction Cells: Challenges and Operational Strategies for Prevention of Salt Precipitation. *Cite This: ACS Energy Lett* **2023**, *8*, 321–331. https://doi.org/10.1021/acsenergylett.2c01885.

(40) Gao, W.; Xu, Y.; Fu, L.; Chang, X.; Xu, B. Experimental Evidence of Distinct Sites for CO2-to-CO and CO Conversion on Cu in the Electrochemical CO2 Reduction Reaction. *Nature Catalysis 2023 6:10* **2023**, *6* (10), 885–894. https://doi.org/10.1038/s41929-023-01002-6.

Table 1. Best-fit parameters extracted from Cu K-edge EXAFS for Cu_2O. R is the radical distance/bond length (with corrected phase shift), CN is coordination number, **σ^2** is the Debye-Waller factor, and ΔE is the energy shift.

Sample	**Fitting structure**	**Shell**	**R** (Å)	**CN**	**σ^2.10^{-3}** (Å)	**ΔE** (eV)
Cu_2O/GDE *Dry*	Cu_2O	Cu-O1	1.95	2.04 (±0.61)	1.19 (±3.77)	4.53 (±4.39)
Flow Cu_2O *CO_2R*	Cu	Cu-Cu	2.53	6.03 (±1.79)	10.72 (±2.91)	1.68 (±2.84)
MEA Cu_2O *CO_2R*	Cu	Cu-Cu	2.54	11.07 (±1.74)	8.64 (±1.41)	3.27 (±1.50)
Flow Cu_2O *COR*	Cu	Cu-Cu	2.52	9.82 (±3.15)	9.21 (±2.94)	1.85 (±3.12)

Table 2. Best-fit parameters extracted from Cu K-edge EXAFS for Cu_2O-Ag. R is the radical distance/bond length (with corrected phase shift), CN is coordination number, **σ^2** is the Debye-Waller factor, and ΔE is the energy shift.

Sample	**Fitting structure**	**Shell**	**R** (Å)	**CN**	**σ^2.10^{-3}** (Å)	**ΔE** (eV)
Cu_2O-Ag/GDE *Dry*	Cu_2O	Cu-O	1.93	1.88 (±0.57)	2.77 (±3.78)	2.80 (±4.54)
Flow Cu_2O-Ag *CO_2R*	Cu_2O	Cu-O	1.97	1.53 (±0.92)	3.62 (±9.73)	9.85 (±7.47)
MEA Cu_2O-Ag *CO_2R*	Cu_2O	Cu-O	1.86	1.33 (±0.56)	2.77 (±3.78)	0.76 (±3.47)
	Cu	Cu-Cu	2.56	3.89 (±1.33)	9.73 (±3.33)	0.76 (±3.47)
Flow Cu_2O-Ag *COR*	Cu	Cu-Cu	2.56	10.14 (±1.26)	9.74 (±1.17)	3.18 (±1.18)

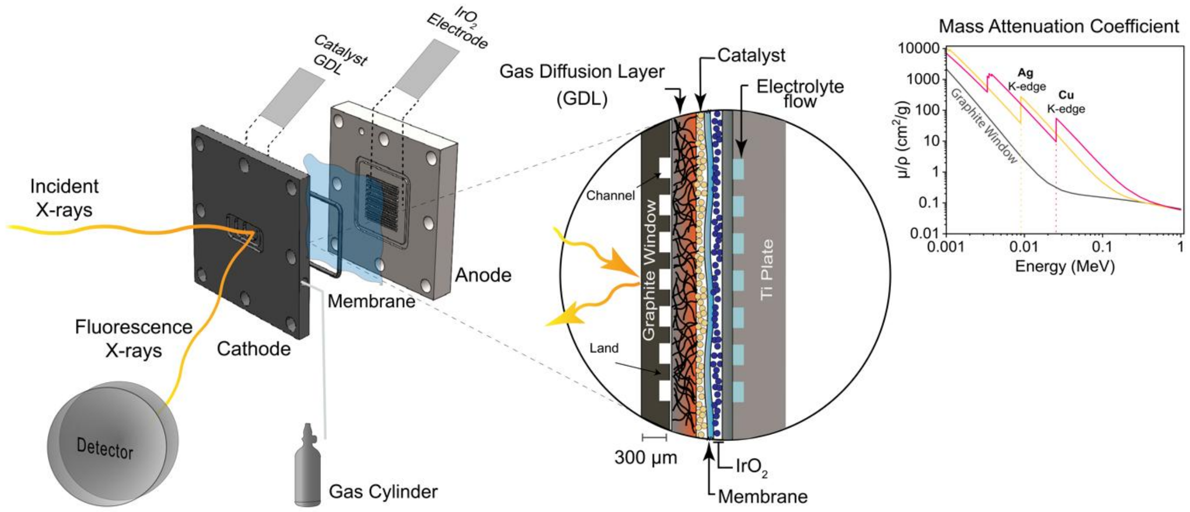

Figure 1. Membrane electrode assembly, MEA, electrolyzer for spectroscopy under reaction environments cell design. (left) front view of the experimental setup with the orientation with respect to the X-ray beam and the detector for XAS measures; (center) a magnified cross-sectional view of the membrane-electrode-assembly sandwiched between graphite plate and Titanium back plate; (right) mass attenuation spectrum (μ/ρ is the mass attenuation coefficient with μ, attenuation coefficient and ρ is the mass density) of graphite (window material), copper (yellow line), and silver (red line) as a function of incident X-ray energy. Notice that the stainless steel cathode back plate is not shown in this figure.

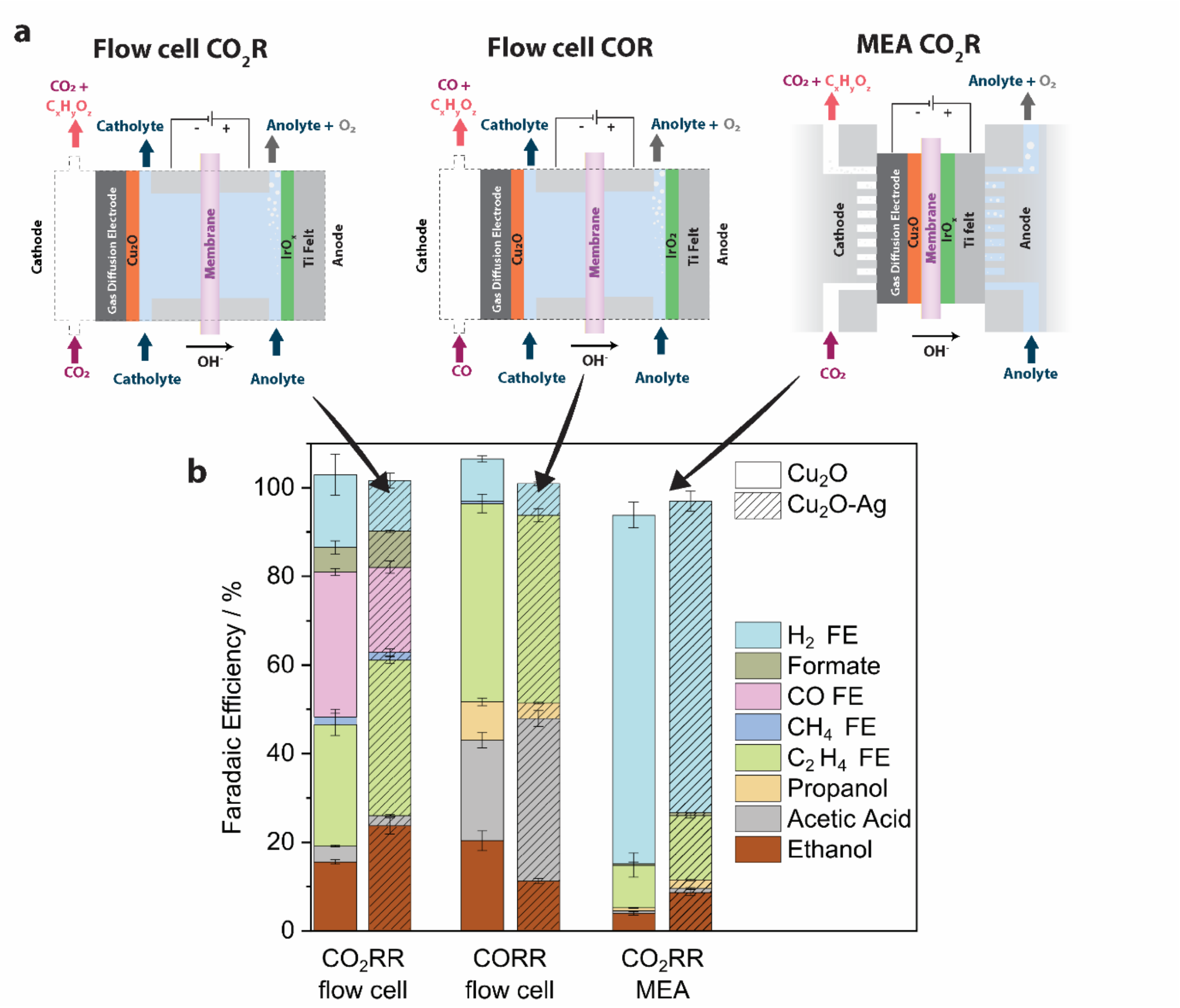

Figure 2. Electrochemical performance of Cu_2O and Cu_2O-Ag. (a) Three schematics showing the reaction configurations for CO_2 reduction in a flow cell (left) using 1 M KOH as catholyte and anolyte and anion exchange membrane (AEM, Fumasep FAA-PK-130), and CO reduction in a flow cell (middle) using 1 M KOH as catholyte and anolyte and AEM (Fumasep FAA-PK-130), and CO_2 reduction in a membrane-electrode-assembly (MEA) cell (right) using 0.1 $KHCO_3$ as anolyte and AEM (Sustainion X37-50), and. (b) Product distribution as measured by gas chromatography for gas products and proton nuclear magnetic resonance for liquid products showing the Faradaic efficiency (FE) of the reaction towards ethanol (CH_3CH_2OH), acetic acid (CH_3COOH), propanol ($CH_3(CH_2)_2OH$), ethylene (H_2CCH_2), methane (CH_4), carbon monoxide (CO), formic acid (HCOOH), and hydrogen (H_2) The solid bars represent experiments on Cu_2O, while the hashed bars are for Cu_2O-Ag.

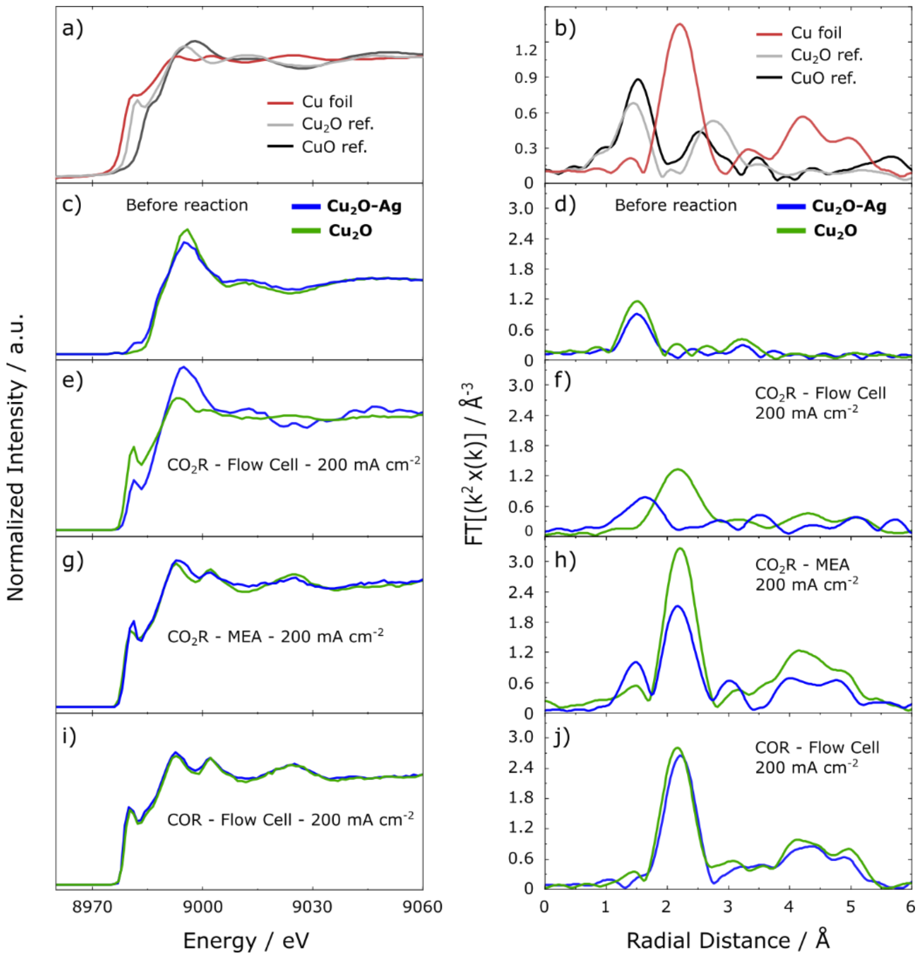

Figure 3. Operando X-ray absorption results. The left panel shows the X-ray absorption near edge structure (XANES), while the right panel shows the phase uncorrected radial distribution function (RDF) derived from extended X-ray absorption fine structures (EXFAS). Panels a) and b) show measurements on standard samples of Cu foil, commercial Cu_2O, and commercial CuO (not under reaction, in dry condition). Panels c-j report measurements on Cu_2O (green curves) and Cu_2O-Ag (blue curves) GDE: c-d) as-prepared samples (in dry condition) ; operando measures under reaction conditions @200 mA cm^{-2}: e-f) in a flow cell and g-h) in a membrane-electrode-assembly under CO_2R and i-j) in a flow cell under COR. All spectra were collected and averaged over 20-30 minutes.

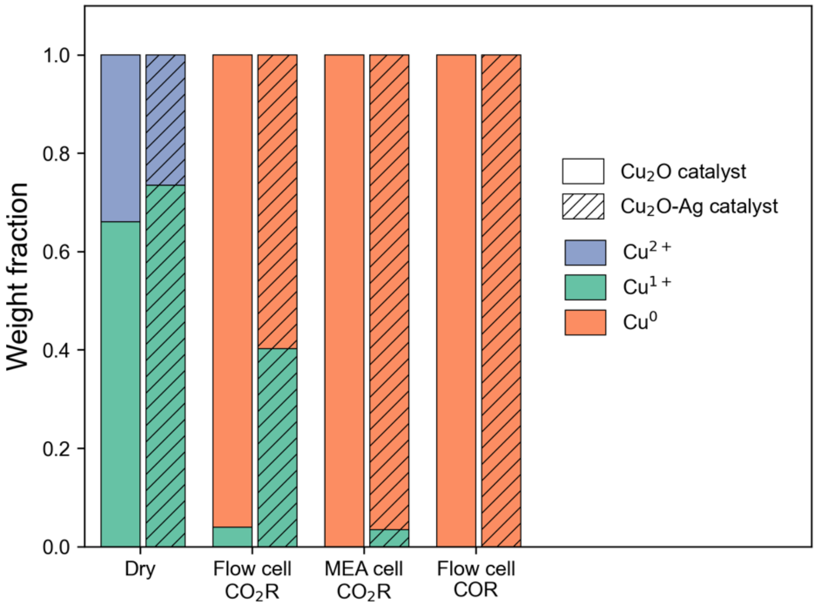

Figure 4. Oxidation state evolution during the reaction. Calculated ratio of Cu oxidation states for as prepared (dry) GDE over the course of reduction at 200 mA cm^{-2} under different reaction conditions obtained by performing linear combination fitting of Cu K-edge X-ray absorption near-edge structure (XANES) spectra.

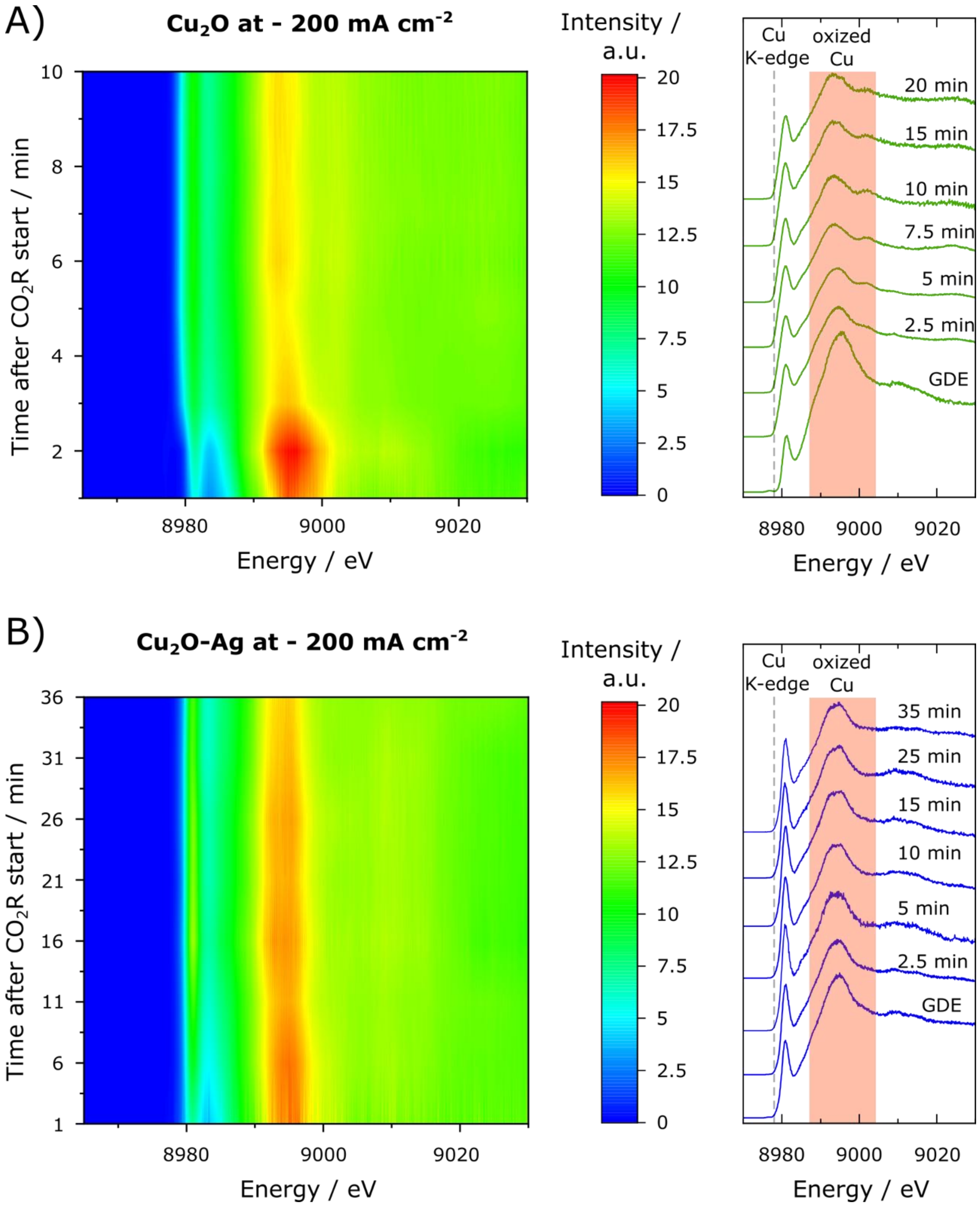

Figure 5. Operando time-resolved X-ray absorption results. The figures show (left) the contour plot of the X-ray fluorescence signal measured every 2 minutes of the CO_2 reduction @ 200 mA cm^{-2} and (right) the stack of X-ray absorption near edge structure (XANES) spectra collected in a flow cell for a) Cu_2O and b) Cu_2O-Ag.